Journal of Magnetic Resonance 275 (2017) 127–136

Contents lists available at ScienceDirect

Journal of Magnetic Resonance

journal homepage: www.elsevier.com/locate/jmr

# Enhanced efficiency of solid-state NMR investigations of energy materials using an external automatic tuning/matching (eATM) robot

Oliver Pecher [a,1], David M. Halat [a,1], Jeongjae Lee [a], Zigeng Liu [a], Kent J. Griffith [a], Marco Braun [b], Clare P. Grey [a,*]

[a] University of Cambridge, Department of Chemistry, Lensfield Road, Cambridge CB2 1EW, UK
[b] NMR Service GmbH, Blumenstr. 70, 99092 Erfurt, Germany

ARTICLE INFO

*Article history:*
Received 10 November 2016
Revised 16 December 2016
Accepted 19 December 2016
Available online 23 December 2016

*Keywords:*
Automation
VOCS
Spin-echo-mapping
*Ex situ* NMR
Li-/Na-ion battery
Energy storage materials

ABSTRACT

We have developed and explored an external automatic tuning/matching (eATM) robot that can be attached to commercial and/or home-built magic angle spinning (MAS) or static nuclear magnetic resonance (NMR) probeheads. Complete synchronization and automation with Bruker and Tecmag spectrometers is ensured via transistor-transistor-logic (TTL) signals. The eATM robot enables an automated "on-the-fly" re-calibration of the radio frequency (rf) carrier frequency, which is beneficial whenever tuning/matching of the resonance circuit is required, *e.g.* variable temperature (VT) NMR, spin-echo mapping (variable offset cumulative spectroscopy, VOCS) and/or *in situ* NMR experiments of batteries. This allows a significant increase in efficiency for NMR experiments outside regular working hours (*e.g.* overnight) and, furthermore, enables measurements of quadrupolar nuclei which would not be possible in reasonable timeframes due to excessively large spectral widths. Additionally, different tuning/matching capacitor (and/or coil) settings for desired frequencies (*e.g.* $^{7}$Li and $^{31}$P at 117 and 122 MHz, respectively, at 7.05 T) can be saved and made directly accessible before automatic tuning/matching, thus enabling automated measurements of multiple nuclei for one sample with no manual adjustment required by the user. We have applied this new eATM approach in static and MAS spin-echo mapping NMR experiments in different magnetic fields on four energy storage materials, namely: (1) paramagnetic $^{7}$Li and $^{31}$P MAS NMR (without manual recalibration) of the Li-ion battery cathode material $LiFePO_4$; (2) paramagnetic $^{17}$O VT-NMR of the solid oxide fuel cell cathode material $La_2NiO_{4+\delta}$; (3) broadband $^{93}$Nb static NMR of the Li-ion battery material $BNb_2O_5$; and (4) broadband static $^{127}$I NMR of a potential Li–air battery product $LiIO_3$. In each case, insight into local atomic structure and dynamics arises primarily from the highly broadened (1–25 MHz) NMR lineshapes that the eATM robot is uniquely suited to collect. These new developments in automation of NMR experiments are likely to advance the application of *in* and *ex situ* NMR investigations to an ever-increasing range of energy storage materials and systems.


## 1. Introduction

The development of solid-state materials for energy storage and conversion (*e.g.* in batteries, supercapacitors, and fuel cells) relies on understanding fundamental relationships between structure and bulk properties such as electronic and ionic conductivity [1–5]. As a direct probe of the environments of atomic nuclei, solid-state nuclear magnetic resonance (NMR) can report on local structure and dynamics [6–8] with relevance to understanding electronic and structural phase transitions [9–12] and ionic diffusion [13–16] on a wide range of time scales.

Among the major challenges in acquiring and interpreting solid-state NMR spectra of functional energy materials are the presence of extremely large anisotropic interactions that cannot be effectively averaged by standard techniques such as magic-angle spinning (MAS) or specialized pulse programs [17,18]. Although these interactions provide important electronic and structural details about the system of interest, they also give rise to broad powder patterns that exceed the NMR probe bandwidth (*ca.* 1 MHz), prohibiting the excitation of the entire spectrum in a single experiment. Acquisition of the overall lineshape thus, in the simplest approach, requires measurements at different radio frequency (rf) carrier frequencies, with frequent and time-

* Corresponding author.
*E-mail address:* cpg27@cam.ac.uk (C.P. Grey).
[1] Authors contributed equally.

http://dx.doi.org/10.1016/j.jmr.2016.12.008
1090-7807/

consuming manual readjustment (tuning and matching) of the rf circuit [19]. Extreme broadening effects may arise for several reasons, which we highlight in turn:

- *Paramagnetic interactions.* Systems containing unpaired electrons are subject to hyperfine interactions such as the isotropic Fermi contact shift and the anisotropic electron–nuclear dipolar coupling interaction, leading to large shifts and broadened lineshapes [20]. These shifts are typically on the order of several thousand ppm, although shifted resonances of nearly 10,000 ppm are not unknown [21,22]. Nonetheless, large paramagnetic shifts and anisotropic broadening values provide important structural information, as they can often be rationalized on the basis of spin-transfer (bond) pathways [23].
- *Quadrupolar coupling interactions.* The coupling of the local electric field gradient (EFG) with the nuclear electric quadrupole moment can lead to exceptionally broad static powder patterns (*ca.* 10 MHz). Particularly problematic quadrupolar nuclei include $^{35/37}$Cl, $^{47/49}$Ti, $^{59}$Co, $^{69/71}$Ga, $^{79/81}$Br, $^{87}$Sr, $^{91}$Zr, $^{93}$Nb, $^{115}$In, and $^{127}$I, with several others (*e.g.* $^{177/179}$Hf, $^{181}$Ta) considered of limited utility due to extreme broadening [18,24–26]. However, broad quadrupolar lineshapes are highly characteristic and correlate sensitively with local geometry.
- *Large NMR shift ranges of heavier spin-½ nuclei.* The NMR spectra of heavier spin-½ nuclides span a wide chemical (and also Knight) shift range [27,28]. Chemical shift ranges (and chemical shift anisotropies, CSAs) of 1000–5000 ppm that are exceptionally responsive to the chemical environment have been reported for $^{109}$Ag, $^{113}$Cd, $^{117/119}$Sn, $^{125}$Te, $^{183}$W, $^{195}$Pt, $^{199}$Hg, and $^{207}$Pb [18,28–30].
- *Variable temperature (VT-NMR) measurements.* The tuning and matching of the probe must be optimized at each temperature in a typical VT-NMR experiment [31–33]. Martin and Zilm [34] ascribe this effect to significant temperature-dependent changes in sample conduction and/or magnetic properties, problems that are also more pronounced for materials that undergo a phase transition over the VT range.
- *Presence of multiple NMR-active nuclei.* Energy storage and conversion materials often contain several NMR-active isotopes. In these systems, a nuclei-switching technique to record multinuclear spectra could be desirable. Examples of previous (manually re-tuned) multinuclear NMR studies potentially validating this approach include $^{7}$Li and $^{31}$P NMR ($\nu_0$ = 117 MHz and 122 MHz at 7.05 T) of the Li-ion battery cathode materials Li*M*PO$_4$ (*M* = Fe, Mn, Co, Ni) [35,36] and the Li solid electrolyte $Li_4SiO_4$–$Li_3PO_4$ [37]; $^{23}$Na, $^{51}$V, and $^{27}$Al NMR ($\nu_0$ = 79.3 MHz, 78.9 MHz, and 78.2 MHz at 7.05 T) of sodium metavanadates [38,39] and glass ceramics [40,41]; and $^{207}$Pb and $^{127}$I NMR ($\nu_0$ = 62.8 MHz and 60.0 MHz at 7.05 T) of the superionic conductor $PbI_2$ [42] and of hybrid halide perovskite materials, *e.g.* $(CH_3NH_3)PbI_3$ [43].

Several specialized techniques have been developed for overcoming these problems and acquiring NMR signals with spectral widths >250 kHz, together referred to as "ultra-wideline NMR spectroscopy" [18]. By far the simplest approach is to sweep the rf carrier frequency, in so-called "frequency-sweep" measurements (also referred to as variable-offset cumulative spectroscopy, VOCS, or spin-echo mapping) [19,44–47]. Alternatively, the use of adiabatic or chirped rf pulses, such as wideline, uniform rate, smooth truncation (WURST) pulses or short high-power adiabatic pulses (SHAP), leads to larger excitation bandwidths at a single carrier frequency, relative to typical high-power rectangular pulses [48–51]. The utility of the adiabatic pulse approach has been extended through sequences such as QCPMG (quadrupolar Carr–Purcell–Meiboom–Gill) echo trains [52–54] and DANTE (Delays Alternating with Nutation for Tailored Excitation) schemes [55–57] to further enhance sensitivity and selectivity in paramagnetic, quadrupolar and large CSA systems. Slow-turning methods, such as the STEAMER (Slow Turning Echo Amplitude Modulation and Echo Reduction) [58] and STREAQI (Slow Turning Reveals Enormous Anisotropic Quadrupolar Interactions) [59] sequences, also resolve broad quadrupolar parameters at a single carrier frequency, although they are often limited in their practical application by requirements of off-magic angle or right-angle spinning. Finally, various hardware-based solutions are available: solenoid microcoils (and magic-angle coil spinning) to access very high rf field amplitudes [60,61]; the use of weak pulsed field gradients in solution-state NMR for broadband decoupling [62,63]; and magnetic field (rather than rf frequency) sweep experiments, using 0.5–1.0 T superconducting sweep coils [64,65] as well as high-field resistive magnets [66].

In this study, we report on the development and application of an external automatic tuning/matching (eATM) robot to repeatedly and accurately recalibrate the resonance circuit without manual intervention, *e.g.* during time-consuming experiments requiring collection of many individual sub-spectra. This eATM device has been developed through an ongoing collaboration between the Grey group at the University of Cambridge (UK) and NMR Service GmbH (Erfurt, Germany), and is now commercially available from the latter [67]. The focus of the present work is the initial application of the eATM prototype to enhance the throughput of solid-state NMR studies of various energy storage systems, as tested through our joint effort. We show that use of the eATM robot significantly boosts the overall collection efficiency of broadband, wideline and VT-NMR experiments, allowing overnight acquisition without direct supervision, and with only minor changes to existing protocols and pulse programs. Rather than replacing existing ultra-wideline NMR schemes, the eATM system accommodates and extends these approaches, as we demonstrate with a combined eATM and WURST-QCPMG experiment.

The eATM robot is physically attached to the tuning/matching rods of the NMR probe and can therefore interface with a broad range of probeheads and NMR spectrometers under static as well as MAS conditions. Previously, a similar device optimized for magnetic resonance imaging (MRI) applications reported by Hwang et al. employed a double-acting hydraulic system [68]. Here, our focus is on acquiring broadband (>1 MHz) NMR spectra of solid-state materials, and an electric motor assembly is instead used to drive the rotation of the tuning/matching rods. Koczor et al. [69] have also recently reported an external remotely-controlled tuning/matching device, which still however requires manual readjustment; in the present work, the eATM system dynamically recalibrates the rf circuit prior to each experiment, with no user input, in response to the forward (fwd) and reflected (rfd) power of a low-power continuous wave (cw) rf pulse.

In this contribution, we describe the initial set-up and practical operation of the eATM robot from a user's point of view, its frequency sweep and recalibration capabilities (Section 4.1), report its use in four proof-of-concept studies of various energy storage and conversion materials (Sections 4.2–4.5), and discuss its applications and future developments (Sections 4.6 and 5). The materials have been chosen to highlight the difficulty in acquiring NMR spectra of systems that are paramagnetic, or contain lineshapes significantly influenced by first- and second-order quadrupolar coupling, in particular under static conditions. In an initial section, we first discuss the technological relevance of these materials as well as open questions regarding structure and dynamics that are amenable to solid-state NMR methods (Section 2).

## 2. Materials systems investigated

### 2.1. $LiFePO_4$

The Li-ion battery cathode material $LiFePO_4$ (LFP) is a well-established model system for understanding Li-ion intercalation reactions. In particular, recent studies of nanosized LFP electrodes have established the fundamental role of metastable kinetic intermediates in enabling high-rate battery operation [70–72]. The formation of these intermediates on charging and discharging can in principle be followed with both $^{7}$Li and $^{31}$P NMR as two distinct probes of the local structure, providing information complementary to X-ray diffraction and microscopy studies [73]. Moreover, as $^{7}$Li and $^{31}$P possess similar Larmor frequencies (117 and 122 MHz, respectively, at 7.05 T), LFP presents an ideal system for testing fully automated nuclei switching. As with other transition-metal phosphates, the $^{7}$Li and $^{31}$P NMR shifts are dominated by large paramagnetic interactions—which can be explicitly quantified through bond pathway decomposition analysis [23]—and thus high-power adiabatic pulses and/or VOCS-like techniques [19] are typically required to map out the broadband $^{7}$Li and $^{31}$P spectra and extract relevant NMR parameters.

### 2.2. $La_2NiO_{4+\delta}$

Solid oxide fuel cells (SOFCs) are solid-state electrochemical conversion devices that traditionally operate at or above 800 °C. An outstanding goal in current SOFC research is to enable functionality at much lower temperatures through the development of materials that show good oxide-ion conduction below 600 °C. Mixed ionic–electronic conductors (MIECs) in particular help to overcome slow oxygen reduction kinetics in electrode operation at lower temperatures.

The perovskite-derived MIEC $La_2NiO_{4+\delta}$ demonstrates remarkably high oxide-ion conductivity and acceptable electronic conductivity at intermediate temperatures, and is recognized as an important candidate cathode material for next-generation SOFCs [74]. The large oxygen excess ($\delta$) in $La_2NiO_{4+\delta}$ arises from non-stoichiometric incorporation of interstitial oxygen; these interstitial defects are highly mobile and a knock-on interstitialcy mechanism has been proposed to account for the oxide-ion conduction [75].

In our group we have employed $La_2NiO_{4+\delta}$ as a model system to extend $^{17}$O MAS solid-state NMR spectroscopic techniques to paramagnetic oxides. Paramagnetic $^{17}$O NMR in the solid-state is virtually unknown, but in a significant advance Kong et al. have shown the utility of spin-echo mapping in acquiring $^{17}$O spectra for transi tion-metal–containing coordination compounds [21]. A similar broadband approach is required for $La_2NiO_{4+\delta}$, where $^{17}$O resonances in both the diamagnetic (interstitial sites) and paramagnetic (axial and equatorial sites) shift ranges are observed, spanning a total of *ca.* 1 MHz (at 16.4 T) [76].

Many studies have employed $^{17}$O solid-state NMR experiments at variable temperatures as a probe of thermally-activated local dynamics in oxide-ion conductors, allowing for calculation of exchange rates and relevant kinetic parameters [13,77]. For $La_2NNiO_{4+\delta}$, an orthorhombic-to-tetragonal phase transition at roughly 130 °C has been reported [78], well within the feasible range of VT-NMR at reasonable MAS rates with standard, commercial probes. Indeed, clear changes in lineshapes and intensity of the $^{17}$O VT-NMR spectra of $La_2NiO_{4+\delta}$ occur as oxide-ion motional processes become activated near 130 °C [76]. From a technical point of view, however, spin-echo mapping experiments become tedious if performed at many different temperatures; approaches to reduce collection time and improve overall experimental efficiency are welcome.

### 2.3. B-$Nb_2O_5$

Niobium oxides [79,80] and Nb-doped compounds [81,82] are emerging in novel energy storage applications, especially for high-power and high-rate applications. While many polymorphs of $Nb_2O_5$ are known, B-$Nb_2O_5$ is a crystallographically interesting model oxide compound due to the presence of a single niobium site with distorted octahedral coordination [83,84]. The structure is monoclinic with *C*2/*c* symmetry; it is composed of edge-sharing octahedral dimers in a corner-sharing network that is related to the titania polymorphs of rutile and $TiO_2$(B). While $^{93}$Nb NMR would seem an ideal technique to study the local distortions of the octahedral niobium site, the large quadrupolar coupling constants associated with this nucleus necessitate the use of more involved ultra-wideline experiments.

### 2.4. $LiIO_3$

Iodine finds use in various energy-related systems, such as the $I^-/I_3^-$ redox couple used in dye-sensitized solar cells [85], lead halide perovskite-based solar cells [43], and as an adduct in Li–$O_2$ batteries [86]. Recently, Liu et al. have shown that addition of lithium iodide to aprotic Li–$O_2$ batteries leads to highly reversible cycling and negligible electrode passivation [86]. In this system, iodine functions as a tunable redox mediator, and iodine oxyanions are speculated to play an important role in the electrochemistry. As $^{127}$I NMR may provide valuable mechanistic insights into this and other systems, we have chosen $LiIO_3$ as a relevant model compound to study the feasibility and utility of ultra-wideline (static) $^{127}$I NMR experiments.

## 3. Experimental section

### 3.1. Sample preparation

#### 3.1.1. $LiFePO_4$

Carbon-coated $LiFePO_4$ was synthesized as previously described [71,73] according to the solid-state reaction of Kobayashi et al. [87]. In detail, 0.556 g lithium carbonate ($Li_2CO_3$, Sigma–Aldrich, 99.997%), 2.681 g iron(II) oxalate dihydrate ($Fe(II)C_2O_4{\cdot}2H_2O$, Sigma–Aldrich, 99%), 1.714 g ammonium dihydrogen phosphate ($NH_4H_2PO_4$, Sigma–Aldrich, 99.999%), and 0.261 g Ketjen black (EC-600JD AkzoNobel) were high energy ball-milled for 40 min to obtain homogeneously mixed precursors. The precursors were then pressed into a pellet and sintered at 600 °C for 6 h under an atmosphere of flowing Ar.

#### 3.1.2. $La_2NiO_{4+\delta}$

Samples of $La_2NiO_{4+\delta}$ were prepared via the solid-state reaction route described previously [88–90]. Stoichiometric amounts of $La_2O_3$ (Alfa Aesar, REacton, 99.999%; pre-dried) and NiO (Aldrich, 99.999%) were mixed in a mortar and pestle, isostatically pressed, sintered in air at 1300 °C for 6–12 h, and ground. Several intermediate sintering and grinding steps were repeated until phase purity was attained, as determined by laboratory powder X-ray diffraction. Samples of $^{17}$O-enriched $La_2NiO_{4+\delta}$ were prepared by heating the as-synthesized powder (0.1–0.3 g) at 1000 °C under an atmosphere of 70% $^{17}O_2$ (Cambridge Isotope Labs, used as received) in a sealed quartz tube for 24 h. Samples were slowly cooled (1 °C min$^{-1}$) from 1000 °C to ensure maximal uptake of $^{17}$O.

#### 3.1.3. B-$Nb_2O_5$

B-$Nb_2O_5$ was prepared *via* thermal oxidation of $NbO_2$ (Alfa Aesar, 99.5+%) at 850 °C for 24 h in air. Rietveld refinement of the

powder X-ray diffraction data [79] showed a minor (*ca.* 2%) contamination from the high-temperature H-$Nb_2O_5$ polymorph.

#### 3.1.4. $LiIO_3$

$LiIO_3$ (97%) was obtained from Sigma-Aldrich. Powder X-ray diffraction did not show any impurities (Supporting Information, Fig. S2) and the sample was used as received.

### 3.2. CASTEP calculations and simulations of NMR spectra

#### 3.2.1. B-$Nb_2O_5$

First principles, periodic density functional theory (DFT) calculations of the NMR parameters of B-$Nb_2O_5$ were performed in the plane-wave code CASTEP (v. 8.0) with ultrasoft pseudopotentials generated 'on-the-fly' [91–94]. The magnetic shielding tensor was calculated within the gauge-including projector-augmented wave (GIPAW) approach while the quadrupolar parameters were calculated directly from the principal components of the electric field gradient at the nucleus. Electron exchange and correlation were treated with the Perdew–Burke–Ernzerhof (PBE) functional within the generalized gradient approximation (GGA) [95]. Calculations were performed with a plane-wave kinetic energy cutoff of 600 eV and k-point sampling of the Brillouin zone with a Monkhorst–Pack grid [96] finer than $2\pi \times 0.06$ Å$^{-1}$. Convergence of isotropic shielding and quadrupolar coupling was checked with respect to both basis-set energy and k-point sampling. Extraction of the Euler angles between the chemical shielding and electric field gradient tensors was performed using MagresView [97]. $LiNbO_3$, with an experimental isotropic shift of –1004 ppm [98], was used to determine the reference shielding for $^{93}$Nb. Euler angle and tensor conventions are given in Supporting Information, Table S1.

#### 3.2.2. $LiIO_3$

A similar computational methodology was adopted as for B-$Nb_2O_5$, with calculations performed using a plane-wave kinetic energy cutoff of 700 eV and k-point sampling with a $8 \times 8 \times 8$ Monkhorst–Pack grid [96]. Ultrasoft pseudopotentials were generated on-the-fly using the zeroth-order regular approximation (ZORA) as implemented in CASTEP [99]. Euler angle and tensor conventions are given in Supporting Information, Table S2. $^{127}$I chemical shielding tensors were referenced to the $^{127}$I chemical shift of NaI (226.71 ppm).

### 3.3. Solid-state NMR experiments

All NMR experiments were performed with the eATM robot attached to the tuning/matching rods of various Bruker probes, and the eATM controller interfaced with Bruker Avance III consoles. The pulse sequences were modified by insertion of a transistor-transistor-logic (TTL) preamble to trigger the synchronization of the auto tuning/matching algorithm (Fig. S1), using a low-power cw pulse of 0.01 W, prior to the start of each data collection. Bruker TopSpin 2.1 and 3.2 were used for raw data processing.

#### 3.3.1. $^7$Li and $^{31}$P MAS NMR of $LiFePO_4$

Solid-state $^7$Li and $^{31}$P MAS NMR experiments were performed on a 7.05 T Bruker Avance III 300 MHz spectrometer ($\nu_0$ = 116.6 MHz and 121.5 MHz for $^7$Li and $^{31}$P, respectively) using a Bruker 2.5 mm HFX MAS probe at a spinning speed of 30 kHz. Spin-echo mapping spectra were recorded at room temperature using a rotor-synchronized Hahn echo pulse sequence of the form $(\pi/2)_x$–$\tau$–$(\pi)_y$–$\tau$–acquire with a pulse length of 4.17 μs ($\pi/2$ pulse, optimized using LiF and $NH_4H_2PO_4$ secondary references) at an inherent rf field strength of *ca.* 60 kHz, and recycle delays of 0.25 s and 50 ms for $^7$Li and $^{31}$P, respectively. For each nucleus, a total of 11 sub-spectra were recorded in steps of 500 ppm (58.3 kHz for $^7$Li and 60.7 kHz for $^{31}$P), from 116.35 to 116.93 MHz for $^7$Li and from 121.62 to 122.22 MHz for $^{31}$P. The $^7$Li and $^{31}$P chemical shifts were referenced to LiF at –1 ppm and $NH_4H_2PO_4$ at 1 ppm, respectively [100,101].

#### 3.3.2. $^{17}$O MAS VT-NMR of $La_2NiO_{4+\delta}$

Solid-state $^{17}$O MAS NMR experiments were carried out on a 16.4 T Bruker Avance III 700 MHz spectrometer ($\nu_0$ = 94.99 MHz for $^{17}$O) using a Bruker 4 mm HXY MAS probe. Spin-echo mapping experiments (step size of 1000 ppm, *i.e.* 95 kHz, with 12 or 13 recorded sub-spectra) were performed at a MAS frequency of 12.5 kHz using a rotor-synchronized Hahn echo pulse sequence of the form $(\pi/6)_x$–$\tau$–$(\pi/3)_y$–$\tau$–acquire, with a pulse length of 2.43 μs ($\pi/6$ for liquid $H_2O$) at an inherent rf field strength of *ca.* 34 kHz, and a recycle delay of 20 ms. Temperature calibration was performed in a separate MAS experiment using the known temperature dependence of the $^{207}$Pb resonance of $Pb(NO_3)_2$, with an accuracy of ±5 °C [102,103]. The $^{17}$O VT-NMR spectra were collected on $^{17}$O-enriched samples packed in $ZrO_2$ rotors with $ZrO_2$ caps. $^{17}$O chemical shifts were externally referenced to $H_2O$ at 0.0 ppm at room temperature.

#### 3.3.3. $^{93}$Nb static NMR of B-$Nb_2O_5$

Solid-state $^{93}$Nb NMR experiments were collected on a 16.4 T Bruker Avance III 700 MHz spectrometer ($\nu_0$ = 171.3 MHz for $^{93}$Nb) using a Bruker 4 mm HXY probe. Static Hahn-echo mapping experiments were recorded at room temperature from 167.8 to 174.8 MHz in 41 steps of *ca.* 1000 ppm (170 kHz). Given the effect of strong quadrupolar coupling on nutation, the rf pulse was directly optimized on the B-$Nb_2O_5$ sample, yielding an effective $\pi/2$ pulse length of 1.0 μs. For each of the 41 spectra, 1664 scans, temporally spaced by a 1 s recycle delay, were co-added and Fourier transformed. $LiNbO_3$, with an isotropic shift of –1004 ppm, was used as a secondary shift reference [98].

#### 3.3.4. $^{127}$I static NMR of $LiIO_3$

Solid-state $^{127}$I NMR experiments were carried out on a 16.4 T Bruker Avance III 700 MHz spectrometer ($\nu_0$ = 140.1 MHz for $^{127}$I) using a Bruker 4 mm HXY MAS probe. Frequency-stepped static spectra were acquired at room temperature using the WURST-QCPMG broadband excitation scheme [51] employing an 8-step phase cycle and a WURST-80 pulse length of 50 μs [49]. For each slice, two spectra were taken with opposing WURST sweep directions to compensate for relaxation during the sweep. An experimentally optimized rf field strength of 10.4 kHz was used, with a frequency step of 0.75 MHz. Spikelet spacing in the QCPMG pulse was 8196 Hz with an echo delay of 50 μs and a recycle delay of 0.5 s. The $^{127}$I spectra were referenced to NaI powder at 227 ppm [104].

## 4. Results and discussion

### 4.1. The eATM system

The eATM system comprises a robot that is placed underneath the probehead (already inside the bore of the magnet) and subsequently connected to an eATM controller (Fig. 1a and b). In addition to the eATM robot itself (Fig. 1c), the equipment includes specially designed rods with adjustable clamping connectors ("fingertips") that can be attached to the outside of the tuning/matching rods of any commercial or homebuilt static or MAS probehead (Fig. 1d). These height-adjustable rods connect to piezoelectric engines inside the cover of the robot (Fig. 1c). After connecting

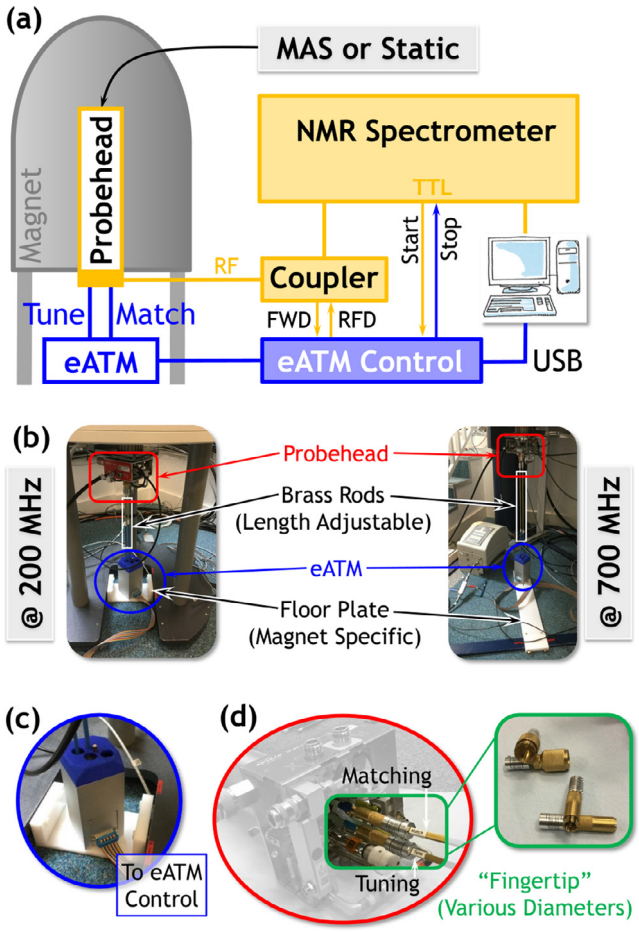


**Fig. 1.** (a) Schematic showing the interplay between the eATM system and NMR spectrometer enabling static or MAS NMR experiments with measurement-synchronized automatic tuning and/or matching. (b) Photos of the eATM robot installed underneath 4.0 mm MAS probeheads at a 200 MHz (4.7 T) and a 700 MHz (16.4 T) magnet. (c) Close-up photograph of the eATM robot during operation. (d) Close-up of the connection between the length-adjustable brass rods and the probehead made *via* clamping connectors ("fingertips"), with various diameters for different types of tuning/matching rods.

the eATM rods to the probe, the robot is itself secured to a plastic floor plate of the appropriate length to prevent self-rotation (Fig. 1b). In this way, the system can fully interface with various probe designs as well as magnets with differences in anti-vibration leg setups and floor plate thicknesses.

The piezoelectric engines are furthermore connected to actuators that are powered by the eATM controller, which makes use of the fwd and rfd power of a low power cw tuning/matching pulse for adjusting the rf carrier to a specific NMR frequency prior to the actual NMR experiment (Fig. 1a). The fwd and rfd power is shunted via a bidirectional coupler, which is incorporated into the rf circuit between the NMR probehead and spectrometer. The eATM control software determines the standing wave ratio (SWR) based on fwd and rfd power at the desired NMR carrier frequency. An automatic ("on-the-fly") recalibration of the rf circuit is then performed algorithmically through robot-controlled changes of the tuning and/or matching capacitors/coils of the probehead, with simultaneous recalculation of the SWR. The loop is repeated until a SWR minimum is reached, corresponding to optimal tuning/matching of the rf circuit to the carrier frequency. The complete automatic tuning/matching procedure (from initial trigger to start of the NMR acquisition) typically requires less than 20 s. Full synchronization of the eATM system and the NMR spectrometer is enabled with TTL input and output signals for start and stop, respectively, *via* a preamble in the applied pulse sequence that defines this synchronization (Supporting Information, Fig. S1a). This preamble for automatic tuning/matching can be readily implemented into any pulse sequence for Bruker and Tecmag consoles and is possible for others.

In the following, we will discuss four applications of the eATM robot in static and MAS spin-echo mapping experiments of different kinds of energy storage and conversion materials.

### 4.2. $^{7}Li$ and $^{31}P$ MAS NMR of $LiFePO_4$

Using the eATM system, a single fully automated measurement of $^{7}Li$ and $^{31}P$ MAS NMR of $LiFePO_4$ has been performed (Fig. 2), comprising 11 sub-spectra in carrier frequency steps of 500 ppm for each nucleus. Given approximately 40 min per sub-spectrum, the entire measurement requires *ca.* 15 h overnight, with no user adjustment required.

As seen in Fig. 2c, this approach allows automatic collection of signal over a broadband range of *ca.* 10 MHz. In practice, the first sub-spectrum for each nucleus was collected by initially recalling the nucleus-specific, pre-saved tuning/matching positions corresponding to the appropriate base carrier frequency (as described in Section 4.6), and then further optimizing the rf circuit by running the eATM autotune algorithm. Subsequent sub-spectra were collected using a typical frequency sweep/VOCS method, as necessitated by the highly broadened (2000–3000 ppm) spinning sideband manifolds for both $^{7}Li$ and $^{31}P$. The paramagnetic lineshapes are in excellent agreement with previous reports [23,105,106], showing that the eATM system enables more efficient acquisition of spectra of several nuclei concurrently, without loss of broadband spectral fidelity, allowing for accurate extraction of hyperfine shifts and dipolar coupling parameters.

### 4.3. $^{17}O$ high-temperature MAS NMR of $La_2NiO_{4+\delta}$

Spin-echo mapped $^{17}O$ NMR spectra of $La_2NiO_{4+\delta}$ at two different sample temperatures, below (79 °C) and above (148 °C) the reported orthorhombic-to-tetragonal phase transition, have been measured (Fig. 3). While the temperatures have been set manually, the collection of NMR spectra is automated via the eATM device. Due to the limited excitation bandwidth of the Hahn echo experiments, each broadband spectrum requires the acquisition and summation of 12–13 sub-spectra with rf carrier frequency step size of 1000 ppm (95 kHz) to reproduce the features of all diamagnetic and paramagnetic oxygen environments accurately. Temperature-dependent changes in the resonance circuit necessitate a probe re-tuning step after heating to 148 °C, which has also been automatically carried out by the eATM robot.

The main changes seen at high temperature (148 °C) are (1) the disappearance of the diamagnetic, lower frequency resonance (535 ppm) assigned to interstitial oxide defects and (2) a narrowing of the resonance at 5400 ppm assigned to equatorial oxygen sites within the perovskite layers. The former is associated with the onset of interstitial motion that leads to a large decrease in the signal intensity; the latter change is attributed to a less distorted (more symmetrical) equatorial environment with a smaller hyperfine shift dispersion, as expected in the high-temperature tetragonal phase [76,107]. Further work is in progress to correlate the low-temperature onset of interstitial oxide-ion dynamics in $La_2NiO_{4+\delta}$ with local structural displacements and distortions of the other (paramagnetic) oxygen environments.

### 4.4. $^{93}Nb$ static NMR of B-$Nb_2O_5$

Despite some favorable properties such as 100% natural abundance and relatively high gyromagnetic ratio, solid-state $^{93}Nb$

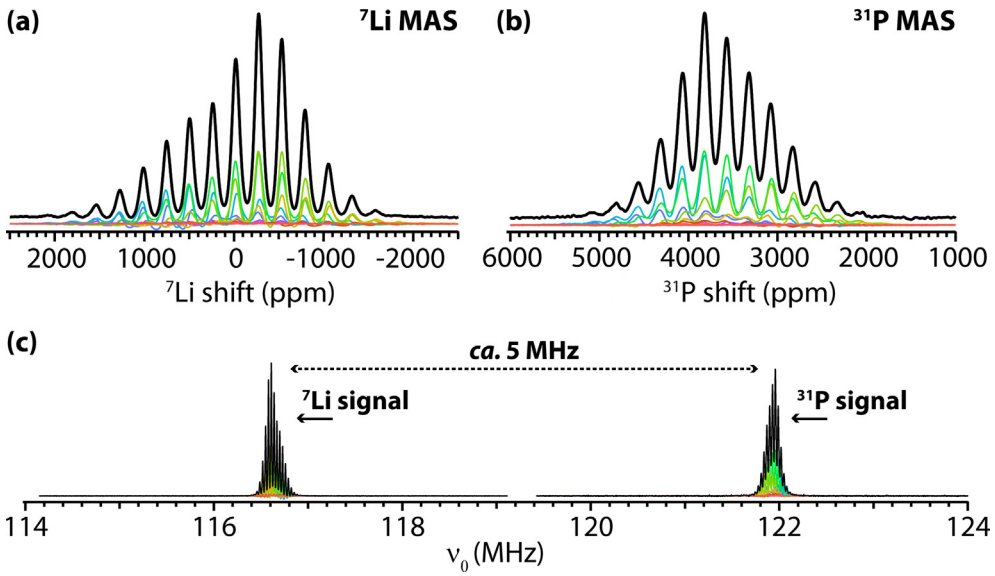


**Fig. 2.** (a) $^{7}$Li MAS NMR spectrum of $LiFePO_4$ at 7.05 T with a MAS speed of 30 kHz (black trace, offset), acquired with spin-echo mapping by summing 11 sub-spectra (colored traces) with rf carrier frequency step size of 500 ppm (58.3 kHz). (b) $^{31}$P MAS NMR spectrum of $LiFePO_4$ under same conditions (black trace, offset), acquired by summing 11 sub-spectra (colored traces) with rf carrier frequency step size of 500 ppm (60.7 kHz). (c) Overall broadband $^{7}$Li and $^{31}$P MAS NMR spectrum of $LiFePO_4$ spanning > 5 MHz, acquired in a single fully automated overnight measurement using the eATM system. (Sub-spectra are depicted as colored traces as in (a) and (b).)

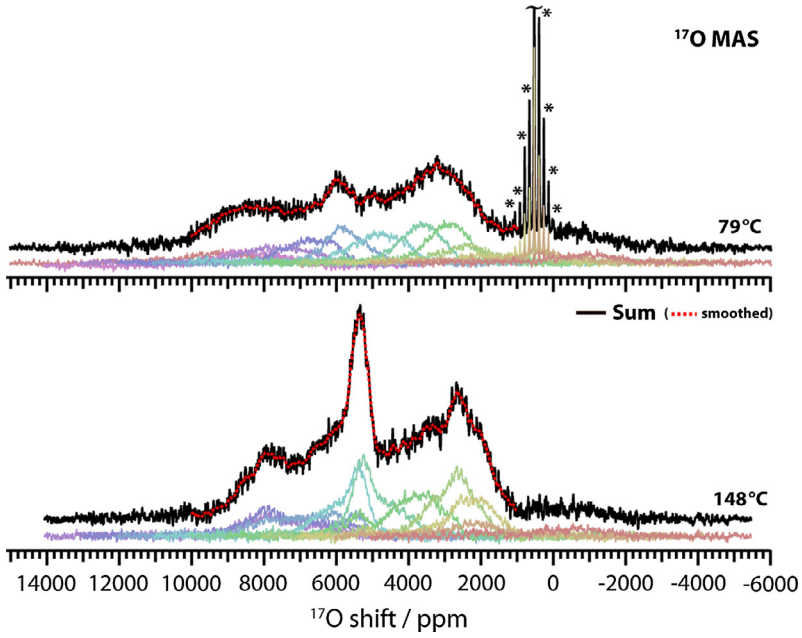


**Fig. 3.** $^{17}$O MAS VT-NMR spectra of $^{17}$O-enriched $La_2NiO_{4+\delta}$, acquired using spin-echo mapping by summing 12–13 sub-spectra (colored traces) with rf carrier frequency step size of 1000 ppm (95 kHz). Spectra were collected at sample temperatures below (79 °C) and above (148 °C) the orthorhombic–tetragonal phase transition of $La_2NiO_{4+\delta}$ (roughly 130 °C). Spectra were obtained at 16.4 T with a MAS rate $\omega_r$ of 12.5 kHz. Asterisks denote spinning sidebands.

NMR studies are limited by the large nuclear quadrupolar coupling constants of distorted niobium environments, which can exceed 100 MHz. Although obtaining acceptable signal-to-noise levels for a single $^{93}$Nb spectrum requires only *ca.* 30 min, manually adjusting the matching and tuning over the course of one day in order to capture the entire quadrupolar lineshape is inefficient and often impractical. Using the eATM device, we obtained the broadband $^{93}$Nb spectrum of B-$Nb_2O_5$ (Fig. 4), spanning a range of 6.97 MHz, by summing 41 individual Hahn-echo sub-spectra automatically acquired in 20 h. Fitting the features and discontinuities of the broadband B-$Nb_2O_5$ $^{93}$Nb NMR spectrum, aided by *ab initio* calculations, enabled the extraction of accurate magnetic shielding and quadrupolar tensors (Supporting Information, Table S1). The fit was performed within the Solid Lineshape Analysis (SOLA) program in TopSpin. Initial parameter values were taken from DFT calculations based on the reported X-ray structure [84]. Given the relatively small CSA, in comparison to the quadrupolar coupling, the relative orientation between these two tensors was fixed at the DFT derived value, while the other parameters were varied to achieve the best fit. Estimated errors are proportional to the sensitivity of the fit to each parameter. These quadrupole tensor values ($C_Q$ = 46(1) MHz, $\eta_Q$ = 0.62(3); *cf.* DFT values of –42.25 MHz/0.60 and –39.1 MHz/0.47 for the fixed and relaxed structures, respectively) reflect the bonding and significant local distortions present in the $NbO_6$ octahedra of this second-order Jahn–Teller distorted $d^0$ niobium(V) oxide.

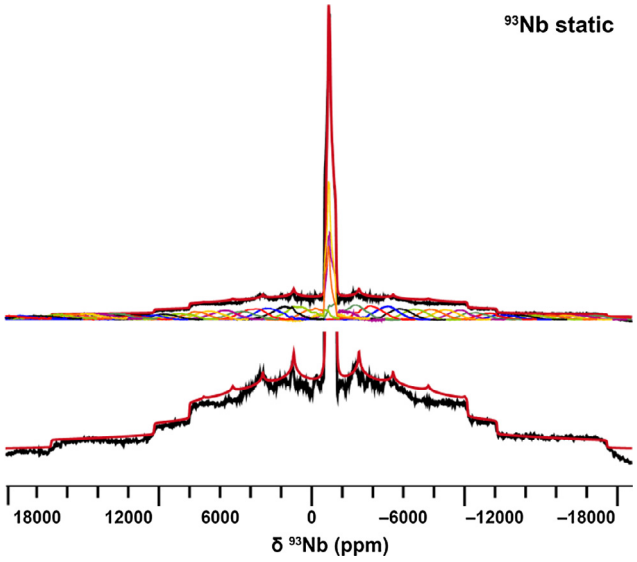


**Fig. 4.** $^{93}$Nb static NMR spectrum of B-$Nb_2O_5$ at 16.4 T ($\nu_0$ = 171.3 MHz). The overall spectrum (black trace) is the summation of 41 individual sub-spectra (colored traces). DFT calculations of NMR tensors and Euler angles were performed to guide the fit (red trace, see main text), using quadrupole coupling parameters of $C_Q$ = 46 (1) MHz and $\eta_Q$ = 0.62(3) (Section 3.2.1; Supporting Information, Table S1). The sub-spectra have been acquired via spin-echo mapping with an rf carrier frequency step size of *ca.* 1000 ppm (170 kHz); the overall spectrum spans *ca.* 7 MHz.

### 4.5. $^{127}$I static NMR of $LiIO_3$

Despite the high natural abundance (100%) and relatively large gyromagnetic ratio ($\gamma = 5.39 \times 10^7$ rad s$^{-1}$ T$^{-1}$) of the $^{127}$I nucleus, both solution and solid-state $^{127}$I NMR studies are rare on account of the extremely strong quadrupolar nature (I = 5/2, Q = −71 fm$^2$) of this nuclide [108]. Most previous solid-state NMR studies have been performed on systems of simple metal iodides such as NaI, $PbI_2$, or alkaline earth metal iodides [42,109]. As systems such as iodates ($IO_3^-$) are expected to exhibit large quadrupole coupling constants due to the lower symmetry about the iodine nucleus, we have tested the applicability of the eATM in measuring very broad, multiple frequency-stepped $^{127}$I spectra. Fig. 5 shows the summed $^{127}$I solid-state NMR spectrum of $LiIO_3$ using the frequency-stepped WURST-QCPMG pulse sequence. Multiple frequency-stepped slices spanning nearly 25 MHz can be automatically acquired by the eATM robot without manual adjustment. To compare to DFT results, the lineshape was simulated with the QUEST software [110] to correctly account for the large quadrupolar interaction. Simulation using DFT-calculated parameters of $C_Q$ = 970.1 MHz and $\eta_Q$ = 0.0 (Supporting Information, Table S2) qualitatively agrees with the ultra-wideline experiment, showing an extremely broad second-order quadrupolar lineshape. In particular, the experimental spectrum exhibits discontinuities at 176 and 153 MHz, in excellent agreement with the relevant subsection of the simulated broadband spectrum. A detailed $^{127}$I NMR study reporting a complete fitting of the experimental spectrum is in progress [111]. Clearly, this investigation shows the utility of eATM experiments in capturing and assigning lineshapes spanning tens of MHz with broadband excitation schemes.

### 4.6. Discussion

Application of the eATM robot is advantageous whenever multiple (automatic) recalibrations of the rf circuit are required, *e.g.* frequency-stepped [44,45,57] (VOCS [14,21,46,112] and/or spin-echo mapping [113–116]) experiments, VT measurements, and/or *in situ* NMR experiments, especially in cases where changes in sample properties can influence the optimal rf setting [73]. Besides straightforward "on-the-fly" automatic tuning/matching to a desired carrier frequency, the eATM system also permits saving different carrier frequencies as tuning/matching servo positions. Upon sending a position-specific TTL signal to the controller *via* the pulse sequence preamble (Supporting Information, Fig. S1b–e), the eATM servos are rotated to the saved values, which is automatically followed by a further recalibration step to the exact rf carrier. This functionality permits fully automated switching between nuclei, provided the pre-set carrier frequencies are within the frequency range of the probe hardware, *e.g.* $^7$Li and $^{31}$P, where $B_0$ = 7.05 T, at 116 and 122 MHz, respectively (Section 4.2).

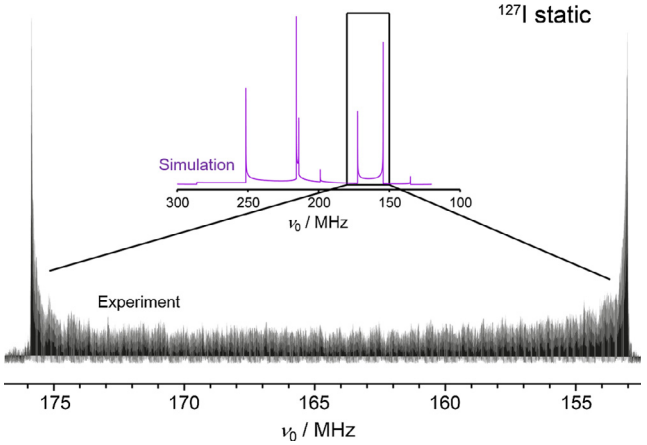


**Fig. 5.** $^{127}$I static NMR spectrum of $LiIO_3$, acquired using WURST-QCPMG. The experimental spectrum (black) is a sum of 64 individual sub-spectra (32 slices). The inset shows a simulation of the NMR spectrum using DFT-calculated NMR parameters of $C_Q$ = 970.1 MHz and $\eta_Q$ = 0.0 (Section 3.2.2; Supporting Information, Table S2).

The flexibility of the system is demonstrated by its integration with a variety of probe and magnet designs, spectrometer systems, and in principle all pulse programs. Moreover, successful operation is observed even for older probes with significant tuning/matching hysteresis of the SWR. The efficiency of the eATM approach is ensured by the speed of the recalibration step, which allows for rapid collection of numerous sub-spectra. This is of particular relevance in the field of energy storage materials, where many *ex situ* samples (*e.g.* as a function of lithiation) may be studied in a single experiment; for measurements spanning a wide spectral range, without the eATM system the overnight magnet time would often be wasted on a single carrier frequency. Finally, the eATM device enables a range of experiments normally considered impractical, such as spanning the entirety of extremely broadened quadrupolar lineshapes, or searching for transitions in nuclear quadrupole resonance (NQR) spectroscopy where the resonance often lies at an unknown position within a *ca.* 10 MHz range.

## 5. Conclusions

We have designed an external automated tuning/matching (eATM) robot system and report on its applications to ultra-wideline and broadband solid-state NMR experiments for a wide variety of probes, consoles, pulse sequences and materials applications. The robot allows for rapid tuning/matching with a broad (>25 MHz) tuning/matching range, permits more efficient frequency-sweep experiments in off-peak hours (especially overnight), and enables automatic multinuclear and VT NMR studies not possible with other ultra-wideline techniques. Ongoing research focuses on the implementation of other adiabatic pulse

sequences analogous to those previously used in ultra-wideline quadrupolar NMR [18] and broadband paramagnetic NMR [57], as well as the combined use of pulsed field gradients (PFG) in performing automated multinuclear diffusion studies. The alternative use of the eATM robot for off-MAS or satellite transition magic angle spinning (STMAS) NMR (by accurately adjusting the magic angle rod) is in progress, as well as the development of automated NQR or hybrid NMR–NQR studies [117]. Furthermore, the combined application of (1) automated sample re-orientation in static NMR experiments using a goniometer with (2) re-calibration of the rf circuit *via* the eATM is likely to become a powerful approach to study (A)BMS effects, which is particularly of interest for energy storage materials [6,118]. Finally we note the potential of "upgrading" static *in situ* NMR probeheads with eATM, given the importance of compensating for changes in battery materials during cycling that influence the optimal tuning/matching settings [73,119]. We conclude that this contribution and future developments in eATM devices are highly promising for extending *in situ* and *ex situ* solid-state NMR studies of energy materials.

## Acknowledgments

We gratefully acknowledge Dr. Nicole M. Trease, Dr. Gunwoo Kim, Joshua M. Stratford, Michael A. Hope, and Dr. Pieter C. M. M. Magusin (all Cambridge, UK) for fruitful discussions. This project has received funding from the European Union's Horizon 2020 research and innovation programme under the Marie Skłodowska-Curie grant agreement No. 655444 (O.P.). D.M.H. acknowledges funding from the Cambridge Commonwealth Trusts. J.L. gratefully acknowledges Trinity College, Cambridge (UK) for funding. K.J.G. gratefully acknowledges funding from the Winston Churchill Foundation of the United States and the Herchel Smith Scholarship. M.B. is the CEO of NMR Service GmbH (Erfurt, Germany), which manufactures the eATM device; M.B. acknowledges funding of the Central Innovation Programme for small and medium-sized enterprises (SMEs; *Zentrales Innovationsprogramm Mittelstand*, ZIM) of the German Federal Ministry of Economic Affairs and Energy (*Bundesministerium für Wirtschaft und Energie*, BMWi) under the Grant No. KF 2845501UWF. DFT calculations were performed on (1) the Darwin Supercomputer of the University of Cambridge High Performance Computing Service (http://www.hpc.cam.ac.uk), provided by Dell Inc. using Strategic Research Infrastructure Funding from the Higher Education Funding Council for England and funding from the Science and Technology Facilities Council and (2) the Center for Functional Nanomaterials cluster, Brookhaven National Laboratory, which is supported by the U.S. Department of Energy, Office of Basic Energy Sciences, under Contract No. DE-AC02-98CH10886.

## Appendix A. Supplementary material

Supplementary data associated with this article can be found, in the online version, at http://dx.doi.org/10.1016/j.jmr.2016.12.008. Data supporting this publication are available at www.repository.cam.ac.uk.

## References

[1] J.-M. Tarascon, M. Armand, Issues and challenges facing rechargeable lithium batteries, Nature 414 (2001) 359–367, http://dx.doi.org/10.1038/35104644.
[2] E.D. Wachsman, K.T. Lee, Lowering the temperature of solid oxide fuel cells, Science 334 (2011) 935–939, http://dx.doi.org/10.1126/science.1204090.
[3] P. Simon, Y. Gogotsi, Materials for electrochemical capacitors, Nat. Mater. 7 (2008) 845–854, http://dx.doi.org/10.1038/nmat2297.
[4] Y.-H. Huang, R.I. Dass, Z.-L. Xing, J.B. Goodenough, Double perovskites as anode materials for solid-oxide fuel cells, Science 312 (2006) 254–257, http://dx.doi.org/10.1126/science.1125877.
[5] J.B. Goodenough, K.-S. Park, The Li-ion rechargeable battery: a perspective, J. Am. Chem. Soc. 135 (2013) 1167–1176, http://dx.doi.org/10.1021/ja3091438.
[6] C.P. Grey, N. Dupré, NMR studies of cathode materials for lithium-ion rechargeable batteries, Chem. Rev. 104 (2004) 4493–4512, http://dx.doi.org/10.1021/cr020734p.
[7] F. Blanc, L. Spencer, G.R. Goward, Encyclopedia of Magnetic Resonance: Quadrupolar NMR of Ionic Conductors, Batteries, and Other Energy-Related Materials, John Wiley & Sons Ltd, Chichester, UK, 2007.
[8] J.H. Kristensen, I. Farnan, Measurement of molecular motion in solids by nuclear magnetic resonance spectroscopy of half-integer quadrupole nuclei, J. Chem. Phys. 114 (2001) 9608–9624, http://dx.doi.org/10.1063/1.1368660.
[9] J. Wu, J.B. Day, K. Franaszczuk, B. Montez, E. Oldfield, A. Wieckowski, P.-A. Vuissoz, J.-P. Ansermet, Recent progress in surface NMR-electrochemistry, J. Chem. Soc., Faraday Trans. 93 (1997) 1017–1026, http://dx.doi.org/10.1039/A603611B.
[10] B.L. Phillips, NMR spectroscopy of phase transitions in minerals, Rev. Mineral. Geochem. 39 (2000) 203–240, http://dx.doi.org/10.2138/rmg.2000.39.08.
[11] Y.-Y. Tong, H.S. Kim, P.K. Babu, P. Waszczuk, A. Wieckowski, E. Oldfield, An NMR investigation of CO tolerance in a Pt/Ru fuel cell catalyst, J. Am. Chem. Soc. 124 (2002) 468–473, http://dx.doi.org/10.1021/ja011729q.
[12] J. Bréger, Y.S. Meng, Y. Hinuma, S. Kumar, K. Kang, Y. Shao-Horn, G. Ceder, C.P. Grey, Effect of high voltage on the structure and electrochemistry of $LiNi_{0.5}Mn_{0.5}O_2$: a joint experimental and theoretical study, Chem. Mater. 18 (2006) 4768–4781, http://dx.doi.org/10.1021/cm060886r.
[13] N. Kim, C.P. Grey, Probing oxygen motion in disordered anionic conductors with $^{17}O$ and $^{51}V$ MAS NMR spectroscopy, Science 297 (2002) 1317–1320, http://dx.doi.org/10.1126/science.1074130.
[14] R.W. Schurko, S. Wi, L. Frydman, Dynamic effects on the powder line shapes of half-integer quadrupolar nuclei: a solid-state NMR Study of $XO_4^-$ groups, J. Phys. Chem. A. 106 (2002) 51–62, http://dx.doi.org/10.1021/jp0130214.
[15] H. Wang, T.K.-J. Köster, N.M. Trease, J. Ségalini, P.-L. Taberna, P. Simon, Y. Gogotsi, C.P. Grey, Real-time NMR studies of electrochemical double-layer capacitors, J. Am. Chem. Soc. 133 (2011) 19270–19273, http://dx.doi.org/10.1021/ja2072115.
[16] A. Kuhn, M. Kunze, P. Sreeraj, H.-D. Wiemhöfer, V. Thangadurai, M. Wilkening, P. Heitjans, NMR relaxometry as a versatile tool to study Li ion dynamics in potential battery materials, Solid State Nucl. Magn. Reson. 42 (2012) 2–8, http://dx.doi.org/10.1016/j.ssnmr.2012.02.001.
[17] A.W. MacGregor, L.A. O'Dell, R.W. Schurko, New methods for the acquisition of ultra-wideline solid-state NMR spectra of spin-½ nuclides, J. Magn. Reson. 208 (2011) 103–113, http://dx.doi.org/10.1016/j.jmr.2010.10.011.
[18] R.W. Schurko, Ultra-wideline solid-state NMR spectroscopy, Acc. Chem. Res. 46 (2013) 1985–1995, http://dx.doi.org/10.1021/ar400045t.
[19] A.J. Pell, R.J. Clément, C.P. Grey, L. Emsley, G. Pintacuda, Frequency-stepped acquisition in nuclear magnetic resonance spectroscopy under magic angle spinning, J. Chem. Phys. 138 (2013) 114201, http://dx.doi.org/10.1063/1.4795001.
[20] I. Bertini, C. Luchinat, G. Parigi, Magnetic susceptibility in paramagnetic NMR, Prog. Nucl. Magn. Reson. Spectrosc. 40 (2002) 249–273, http://dx.doi.org/10.1016/S0079-6565(02)00002-X.
[21] X. Kong, V.V. Terskikh, R.L. Khade, L. Yang, A. Rorick, Y. Zhang, P. He, Y. Huang, G. Wu, Solid-state $^{17}O$ NMR spectroscopy of paramagnetic coordination compounds, Angew. Chem., Int. Ed. 54 (2015) 4753–4757, http://dx.doi.org/10.1002/anie.201409888.
[22] C.P. Grey, C.M. Dobson, A.K. Cheetham, R.J.B. Jakeman, Studies of rare-earth stannates by $^{119}Sn$ MAS NMR. The use of paramagnetic shift probes in the solid state, J. Am. Chem. Soc. 111 (1989) 505–511, http://dx.doi.org/10.1021/ja00184a017.
[23] R.J. Clément, A.J. Pell, D.S. Middlemiss, F.C. Strobridge, J.K. Miller, M.S. Whittingham, L. Emsley, C.P. Grey, G. Pintacuda, Spin-transfer pathways in paramagnetic lithium transition-metal phosphates from combined broadband isotropic solid-state MAS NMR spectroscopy and DFT calculations, J. Am. Chem. Soc. 134 (2012) 17178–17185, http://dx.doi.org/10.1021/ja306876u.
[24] S.E. Ashbrook, S. Sneddon, New methods and applications in solid-state NMR spectroscopy of quadrupolar nuclei, J. Am. Chem. Soc. 136 (2014) 15440–15456, http://dx.doi.org/10.1021/ja504734p.
[25] K.E. Johnston, C.A. O'Keefe, R.M. Gauvin, J. Trébosc, L. Delevoye, J.-P. Amoureux, N. Popoff, M. Taoufik, K. Oudatchin, R.W. Schurko, A study of transition-metal organometallic complexes combining $^{35}Cl$ solid-state NMR spectroscopy and $^{35}Cl$ NQR spectroscopy and first-principles DFT calculations, Chem. Eur. J. 19 (2013) 12396–12414, http://dx.doi.org/10.1002/chem.201301268.
[26] P. He, B.E.G. Lucier, V.V. Terskikh, Q. Shi, J. Dong, Y. Chu, A. Zheng, A. Sutrisno, Y. Huang, Spies within metal-organic frameworks: investigating metal centers using solid-state NMR, J. Phys. Chem. C. 118 (2014) 23728–23744, http://dx.doi.org/10.1021/jp5063868.
[27] C.J. Jameson, H.S. Gutowsky, Calculation of chemical shifts. I. General formulation and the Z dependence, J. Chem. Phys. 40 (1964) 1714–1724, http://dx.doi.org/10.1063/1.1725387.
[28] A.-C. Pöppler, J.-P. Demers, M. Malon, A.P. Singh, H.W. Roesky, Y. Nishiyama, A. Lange, Ultrafast magic-angle spinning: benefits for the acquisition of ultrawide-line NMR spectra of heavy spin-½ nuclei, ChemPhysChem 17 (2016) 812–816, http://dx.doi.org/10.1002/cphc.201501136.

[29] P.J. Domaille, The 1- and 2-dimensional tungsten-183 and vanadium-51 NMR characterization of isopolymetalates and heteropolymetalates, J. Am. Chem. Soc. 106 (1984) 7677–7687, http://dx.doi.org/10.1021/ja00337a004.

[30] D. Larink, M.T. Rinke, H. Eckert, Mixed network former effects in tellurite glass systems: structure/property correlations in the system $(Na_2O)_{1/3}[(2TeO_2)_x(P_2O_5)_{1-x}]_{2/3}$, J. Phys. Chem. C. 119 (2015) 17539–17551, http://dx.doi.org/10.1021/acs.jpcc.5b04074.

[31] G.J.M.P. Van Moorsel, E.R.H. Van Eck, C.P. Grey, $Pr_2Sn_2O_7$ and $Sm_2Sn_2O_7$ as high-temperature shift thermometers in variable-temperature $^{119}Sn$ MAS NMR, J. Magn. Reson. Ser. A 113 (1995) 159–163, http://dx.doi.org/10.1006/jmra.1995.1075.

[32] J.F. Haw, Variable-temperature solid-state NMR spectroscopy, Anal. Chem. 60 (1988) 559A–570A, http://dx.doi.org/10.1021/ac00160a001.

[33] D.R. Kinney, I.S. Chuang, G.E. Maciel, Water and the silica surface as studied by variable-temperature high-resolution proton NMR, J. Am. Chem. Soc. 115 (1993) 6786–6794, http://dx.doi.org/10.1021/ja00068a041.

[34] R.W. Martin, K.W. Zilm, Variable temperature system using vortex tube cooling and fiber optic temperature measurement for low temperature magic angle spinning NMR, J. Magn. Reson. 168 (2004) 202–209, http://dx.doi.org/10.1016/j.jmr.2004.03.002.

[35] S.L. Wilcke, Y.-J. Lee, E.J. Cairns, J.A. Reimer, Covalency measurements via NMR in lithium metal phosphates, Appl. Magn. Reson. 32 (2007) 547–563, http://dx.doi.org/10.1007/s00723-007-0032-1.

[36] F.C. Strobridge, R.J. Clément, M. Leskes, D.S. Middlemiss, O.J. Borkiewicz, K.M. Wiaderek, K.W. Chapman, P.J. Chupas, C.P. Grey, Identifying the structure of the intermediate, $Li_{2/3}CoPO_4$, formed during electrochemical cycling of $LiCoPO_4$, Chem. Mater. 26 (2014) 6193–6205, http://dx.doi.org/10.1021/cm502680w.

[37] Y. Deng, C. Eames, J.-N. Chotard, F. Lalère, V. Seznec, S. Emge, O. Pecher, C.P. Grey, C. Masquelier, M.S. Islam, Structural and mechanistic insights into fast lithium-ion conduction in $Li_4SiO_4$–$Li_3PO_4$ solid electrolytes, J. Am. Chem. Soc. 137 (2015) 9136–9145, http://dx.doi.org/10.1021/jacs.5b04444.

[38] J. Skibsted, N.C. Nielsen, H. Bildsøe, H.J. Jakobsen, Magnitudes and relative orientation of vanadium-51 quadrupole coupling and anisotropic shielding tensors in metavanadates and potassium vanadium oxide ($KV_3O_8$) from vanadium-51 MAS NMR spectra. Sodium-23 quadrupole coupling parameters for $\alpha$- and $\beta$-$NaVO_3$, J. Am. Chem. Soc. 115 (1993) 7351–7362, http://dx.doi.org/10.1021/ja00069a038.

[39] H. Takeda, M. Itoh, H. Sakurai, Magnetic frustration effect in the multi-band vanadate $NaV_2O_4$, J. Phys.: Conf. Ser. 273 (2011) 12142, http://dx.doi.org/10.1088/1742-6596/273/1/012142.

[40] I. Abrahams, K. Franks, G.E. Hawkes, G. Philippou, J. Knowles, P. Bodart, T. Nunes, $^{23}Na$, $^{27}Al$ and $^{31}P$ NMR and X-ray powder diffraction study of Na/Ca/Al phosphate glasses and ceramics, J. Mater. Chem. 7 (1997) 1573–1580, http://dx.doi.org/10.1039/A608325K.

[41] C. Bessada, E.M. Anghel, $^{11}B$, $^{23}Na$, $^{27}Al$, and $^{19}F$ NMR study of solid and molten $Na_3AlF_6$–$Na_2B_4O_7$, Inorg. Chem. 42 (2003) 3884–3890, http://dx.doi.org/10.1021/ic026074o.

[42] R.E. Taylor, P.A. Beckmann, S. Bai, C. Dybowski, $^{127}I$ and $^{207}Pb$ solid-state NMR spectroscopy and nuclear spin relaxation in $PbI_2$: a preliminary study, J. Phys. Chem. C. 118 (2014) 9143–9153, http://dx.doi.org/10.1021/jp5023423.

[43] I. Moudrakovski, A. Senocrate, T.-Y. Yang, G. Gregori, J. Maier, Solid state NMR and NQR in methylammonium lead iodide, in: 58th Rocky Mountain Conference on Magnetic Resonance, Breckenridge, Colorado, 2016.

[44] Y.Y. Tong, Nuclear spin-echo Fourier-transform mapping spectroscopy for broad NMR lines in solids, J. Magn. Reson. Ser. A. 119 (1996) 22–28, http://dx.doi.org/10.1006/jmra.1996.0047.

[45] H.E. Rhodes, P.-K. Wang, H.T. Stokes, C.P. Slichter, J.H. Sinfelt, NMR of platinum catalysts. I. Line shapes, Phys. Rev. B. 26 (1982) 3559–3568, http://dx.doi.org/10.1103/PhysRevB.26.3559.

[46] D. Massiot, I. Farnan, N. Gautier, D. Trumeau, A. Trokiner, J.P. Coutures, $^{71}Ga$ and $^{69}Ga$ nuclear magnetic resonance study of $\beta$-$Ga_2O_3$: resolution of four- and six-fold coordinated Ga sites in static conditions, Solid State Nucl. Magn. Reson. 4 (1995) 241–248, http://dx.doi.org/10.1016/0926-2040(95)00002-8.

[47] D. Bräunling, O. Pecher, D.M. Trots, A. Senyshyn, D.A. Zherebtsov, F. Haarmann, R. Niewa, Synthesis, crystal structure and lithium motion of $Li_8SeN_2$ and $Li_8TeN_2$, Z. Anorg. Allg. Chem. 636 (2010) 936–946, http://dx.doi.org/10.1002/zaac.201000002.

[48] E. Kupce, R. Freeman, Adiabatic pulses for wideband inversion and broadband decoupling, J. Magn. Reson. Ser. A. 115 (1995) 273–276, http://dx.doi.org/10.1006/jmra.1995.1179.

[49] R. Bhattacharyya, L. Frydman, Quadrupolar nuclear magnetic resonance spectroscopy in solids using frequency-swept echoing pulses, J. Chem. Phys. 127 (2007) 194503, http://dx.doi.org/10.1063/1.2793783.

[50] G. Kervern, G. Pintacuda, L. Emsley, Fast adiabatic pulses for solid-state NMR of paramagnetic systems, Chem. Phys. Lett. 435 (2007) 157–162, http://dx.doi.org/10.1016/j.cplett.2006.12.056.

[51] L.A. O'Dell, A.J. Rossini, R.W. Schurko, Acquisition of ultra-wideline NMR spectra from quadrupolar nuclei by frequency stepped WURST–QCPMG, Chem. Phys. Lett. 468 (2009) 330–335, http://dx.doi.org/10.1016/j.cplett.2008.12.044.

[52] F.H. Larsen, H.J. Jakobsen, P.D. Ellis, N.C. Nielsen, Sensitivity-enhanced quadrupolar-echo NMR of half-integer quadrupolar nuclei. Magnitudes and relative orientation of chemical shielding and quadrupolar coupling tensors, J. Phys. Chem. A. 101 (1997) 8597–8606, http://dx.doi.org/10.1021/jp971547b.

[53] I. Hung, A.J. Rossini, R.W. Schurko, Application of the Carr–Purcell Meiboom–Gill pulse sequence for the acquisition of solid-state NMR spectra of spin-½ nuclei, J. Phys. Chem. A 108 (2004) 7112–7120, http://dx.doi.org/10.1021/jp0401123.

[54] R. Siegel, T.T. Nakashima, R.E. Wasylishen, Application of multiple-pulse experiments to characterize broad NMR chemical-shift powder patterns from spin-½ nuclei in the solid state, J. Phys. Chem. B. 108 (2004) 2218–2226, http://dx.doi.org/10.1021/jp031048c.

[55] V. Vitzthum, M.A. Caporini, S. Ulzega, G. Bodenhausen, Broadband excitation and indirect detection of nitrogen-14 in rotating solids using Delays Alternating with Nutation (DANTE), J. Magn. Reson. 212 (2011) 234–239, http://dx.doi.org/10.1016/j.jmr.2011.06.013.

[56] D. Carnevale, V. Vitzthum, O. Lafon, J. Trébosc, J.-P. Amoureux, G. Bodenhausen, Broadband excitation in solid-state NMR of paramagnetic samples using Delays Alternating with Nutation for Tailored Excitation ("Para-DANTE"), Chem. Phys. Lett. 553 (2012) 68–76, http://dx.doi.org/10.1016/j.cplett.2012.09.056.

[57] A.J. Pell, G. Pintacuda, Broadband solid-state MAS NMR of paramagnetic systems, Prog. Nucl. Magn. Reson. Spectrosc. 84–85 (2015) 33–72, http://dx.doi.org/10.1016/j.pnmrs.2014.12.002.

[58] E.A. Hill, J.P. Yesinowski, A slow-turning method for measuring large anisotropic interactions in inhomogeneously broadened nuclear magnetic resonance spectra, J. Chem. Phys. 106 (1997) 8650–8659, http://dx.doi.org/10.1063/1.473926.

[59] J. Persons, G.S. Harbison, Slow turning reveals enormous quadrupolar interactions (STREAQI), J. Magn. Reson. 186 (2007) 347–351, http://dx.doi.org/10.1016/j.jmr.2007.03.002.

[60] K. Yamauchi, J.W.G. Janssen, A.P.M. Kentgens, Implementing solenoid microcoils for wide-line solid-state NMR, J. Magn. Reson. 167 (2004) 87–96, http://dx.doi.org/10.1016/j.jmr.2003.12.003.

[61] D. Sakellariou, G.L. Goff, J.-F. Jacquinot, High-resolution, high-sensitivity NMR of nanolitre anisotropic samples by coil spinning, Nature 447 (2007) 694–697, http://dx.doi.org/10.1038/nature05897.

[62] K. Zangger, H. Sterk, Homonuclear broadband-decoupled NMR spectra, J. Magn. Reson. 124 (1997) 486–489, http://dx.doi.org/10.1006/jmre.1996.1063.

[63] A.J. Pell, J. Keeler, Two-dimensional J-spectra with absorption-mode lineshapes, J. Magn. Reson. 189 (2007) 293–299, http://dx.doi.org/10.1016/j.jmr.2007.09.002.

[64] I.J.F. Poplett, M.E. Smith, Field sweep broadline NMR spectroscopy, Solid State Nucl. Magn. Reson. 11 (1998) 211–214, http://dx.doi.org/10.1016/S0926-2040(97)00110-0.

[65] G.J. Rees, S.T. Orr, L.O. Barrett, J.M. Fisher, J. Houghton, G.H. Spikes, B.R.C. Theobald, D. Thompsett, M.E. Smith, J.V. Hanna, Characterisation of platinum-based fuel cell catalyst materials using $^{195}Pt$ wideline solid state NMR, Phys. Chem. Chem. Phys. 15 (2013) 17195–17207, http://dx.doi.org/10.1039/C3CP52268G.

[66] I. Hung, K. Shetty, P.D. Ellis, W.W. Brey, Z. Gan, High-field QCPMG NMR of large quadrupolar patterns using resistive magnets, Solid State Nucl. Magn. Reson. 36 (2009) 159–163, http://dx.doi.org/10.1016/j.ssnmr.2009.10.001.

[67] NMR Service GmbH (Erfurt, Germany), www.nmr-service.de; email: m.braun@nmr-service.de.

[68] F. Hwang, D.I. Hoult, Automatic probe tuning and matching, Magn. Reson. Med. 39 (1998) 214–222, http://dx.doi.org/10.1002/mrm.1910390208.

[69] B. Koczor, I. Sedyó, J. Rohonczy, An alternative solution for computer controlled tuning and matching of existing NMR probes, J. Magn. Reson. 259 (2015) 179–185, http://dx.doi.org/10.1016/j.jmr.2015.08.017.

[70] X. Zhang, M. van Hulzen, D.P. Singh, A. Brownrigg, J.P. Wright, N.H. van Dijk, M. Wagemaker, Rate-induced solubility and suppression of the first-order phase transition in olivine $LiFePO_4$, Nano Lett. 14 (2014) 2279–2285, http://dx.doi.org/10.1021/nl404285y.

[71] H. Liu, F.C. Strobridge, O.J. Borkiewicz, K.M. Wiaderek, K.W. Chapman, P.J. Chupas, C.P. Grey, Capturing metastable structures during high-rate cycling of $LiFePO_4$ nanoparticle electrodes, Science 344 (2014) 1252817, http://dx.doi.org/10.1126/science.1252817.

[72] J. Lim, Y. Li, D.H. Alsem, H. So, S.C. Lee, P. Bai, D.A. Cogswell, X. Liu, N. Jin, Y. Yu, N.J. Salmon, D.A. Shapiro, M.Z. Bazant, T. Tyliszczak, W.C. Chueh, Origin and hysteresis of lithium compositional spatiodynamics within battery primary particles, Science 353 (2016) 566–571, http://dx.doi.org/10.1126/science.aaf4914.

[73] O. Pecher, P.M. Bayley, H. Liu, Z. Liu, N.M. Trease, C.P. Grey, Automatic Tuning Matching Cycler (ATMC) *in situ* NMR spectroscopy as a novel approach for real-time investigations of Li- and Na-ion batteries, J. Magn. Reson. 265 (2016) 200–209, http://dx.doi.org/10.1016/j.jmr.2016.02.008.

[74] A. Aguadero, L. Fawcett, S. Taub, R. Woolley, K.-T. Wu, N. Xu, J.A. Kilner, S.J. Skinner, Materials development for intermediate-temperature solid oxide electrochemical devices, J. Mater. Sci. 47 (2012) 3925–3948, http://dx.doi.org/10.1007/s10853-011-6213-1.

[75] A. Chroneos, D. Parfitt, J.A. Kilner, R.W. Grimes, Anisotropic oxygen diffusion in tetragonal $La_2NiO_{4+\delta}$: molecular dynamics calculations, J. Mater. Chem. 20 (2010) 266–270, http://dx.doi.org/10.1039/B917118E.

[76] D.M. Halat, R. Dervişoğlu, G. Kim, M.T. Dunstan, F. Blanc, D.S. Middlemiss, C.P. Grey, Probing oxide-ion mobility in the mixed ionic-electronic conductor $La_2NiO_{4+\delta}$ by solid-state $^{17}O$ MAS NMR spectroscopy, J. Am. Chem. Soc. 138 (2016) 11958–11969, http://dx.doi.org/10.1021/jacs.6b07348.

[77] M.R. Hampson, J.S.O. Evans, P. Hodgkinson, Characterization of oxygen dynamics in $ZrW_2O_8$, J. Am. Chem. Soc. 127 (2005) 15175–15181, http://dx.doi.org/10.1021/ja054063z.

[78] A. Aguadero, J.A. Alonso, M.J. Martínez-Lope, M.T. Fernández-Díaz, M.J. Escudero, L. Daza, *In situ* high temperature neutron powder diffraction study of oxygen-rich $La_2NiO_{4+\delta}$ in air: correlation with the electrical behaviour, J. Mater. Chem. 16 (2006) 3402–3408, http://dx.doi.org/10.1039/B605886H.

[79] K.J. Griffith, A.C. Forse, J.M. Griffin, C.P. Grey, High-rate intercalation without nanostructuring in metastable $Nb_2O_5$ bronze phases, J. Am. Chem. Soc. 138 (2016) 8888–8899, http://dx.doi.org/10.1021/jacs.6b04345.

[80] N. Kumagai, Y. Koishikawa, S. Komaba, N. Koshiba, Thermodynamics and kinetics of lithium intercalation into $Nb_2O_5$ electrodes for a 2 V rechargeable lithium battery, J. Electrochem. Soc. 146 (1999) 3203–3210, http://dx.doi.org/10.1149/1.1392455.

[81] G. Sahasrabudhe, J. Krizan, S.L. Bergman, R.J. Cava, J. Schwartz, Million-fold increase of the conductivity in $TiO_2$ rutile through 3% niobium incorporation, Chem. Mater. 28 (2016) 3630–3633, http://dx.doi.org/10.1021/acs.chemmater.6b02031.

[82] M. Fehse, S. Cavaliere, P.E. Lippens, I. Savych, A. Iadecola, L. Monconduit, D.J. Jones, J. Rozière, F. Fischer, C. Tessier, L. Stievano, Nb-doped $TiO_2$ nanofibers for lithium ion batteries, J. Phys. Chem. C. 117 (2013) 13827–13835, http://dx.doi.org/10.1021/jp402498p.

[83] F. Laves, W. Petter, H. Wulf, Die Kristallstruktur von $\zeta$-$Nb_2O_5$, Naturwissenschaften 51 (1964) 633–634, http://dx.doi.org/10.1007/BF00623669.

[84] T.S. Ercit, Refinement of the structure of $\zeta$-$Nb_2O_5$ and its relationship to the rutile and thoreaulite structures, Mineral. Petrol. 43 (1991) 217–223, http://dx.doi.org/10.1007/BF01166893.

[85] G. Boschloo, A. Hagfeldt, Characteristics of the iodide/triiodide redox mediator in dye-sensitized solar cells, Acc. Chem. Res. 42 (2009) 1819–1826, http://dx.doi.org/10.1021/ar900138m.

[86] T. Liu, M. Leskes, W. Yu, A.J. Moore, L. Zhou, P.M. Bayley, G. Kim, C.P. Grey, Cycling Li-$O_2$ batteries *via* LiOH formation and decomposition, Science 350 (2015) 530–533, http://dx.doi.org/10.1126/science.aac7730.

[87] G. Kobayashi, S. Nishimura, M.-S. Park, R. Kanno, M. Yashima, T. Ida, A. Yamada, Isolation of solid solution phases in size-controlled $Li_xFePO_4$ at room temperature, Adv. Funct. Mater. 19 (2009) 395–403, http://dx.doi.org/10.1002/adfm.200801522.

[88] M. Sayer, P. Odier, Electrical properties and stoichiometry in $La_2NiO_4$, J. Solid State Chem. 67 (1987) 26–36, http://dx.doi.org/10.1016/0022-4596(87)90334-3.

[89] H. Tamura, A. Hayashi, Y. Ueda, Phase diagram of $La_2NiO_{4+\delta}$ ($0 \leqslant \delta \leqslant 0.18$): I. Phase at room temperature and phase transition above $\delta = 0.15$, Phys. C. 216 (1993) 83–88, http://dx.doi.org/10.1016/0921-4534(93)90636-5.

[90] H.L. Zhang, X.S. Wu, C.S. Chen, W. Liu, Excess oxygen ordering in the $La_2NiO_{4+\delta}$ system studied by low-frequency internal friction, Phys. Rev. B. 71 (2005) 64422, http://dx.doi.org/10.1103/PhysRevB.71.064422.

[91] S.J. Clark, M.D. Segall, C.J. Pickard, P.J. Hasnip, M.I.J. Probert, K. Refson, M.C. Payne, First principles methods using CASTEP, Z. Kristallogr. - Cryst. Mater. 220 (2005), http://dx.doi.org/10.1524/zkri.220.5.567.65075.

[92] C.J. Pickard, F. Mauri, All-electron magnetic response with pseudopotentials: NMR chemical shifts, Phys. Rev. B. 63 (2001) 245101, http://dx.doi.org/10.1103/PhysRevB.63.245101.

[93] J.R. Yates, C.J. Pickard, F. Mauri, Calculation of NMR chemical shifts for extended systems using ultrasoft pseudopotentials, Phys. Rev. B. 76 (2007) 24401, http://dx.doi.org/10.1103/PhysRevB.76.024401.

[94] M. Profeta, F. Mauri, C.J. Pickard, Accurate first principles prediction of $^{17}O$ NMR parameters in $SiO_2$: assignment of the Zeolite Ferrierite spectrum, J. Am. Chem. Soc. 125 (2003) 541–548, http://dx.doi.org/10.1021/ja027124r.

[95] J.P. Perdew, K. Burke, M. Ernzerhof, Generalized gradient approximation made simple, Phys. Rev. Lett. 77 (1996) 3865–3868, http://dx.doi.org/10.1103/PhysRevLett. 77.3865.

[96] H.J. Monkhorst, J.D. Pack, Special points for Brillouin-zone integrations, Phys. Rev. B. 13 (1976) 5188–5192, http://dx.doi.org/10.1103/PhysRevB.13.5188.

[97] S. Sturniolo, T.F.G. Green, R.M. Hanson, M. Zilka, K. Refson, P. Hodgkinson, S.P. Brown, J.R. Yates, Visualization and processing of computed solid-state NMR parameters: MagresView and MagresPython, Solid State Nucl. Magn. Reson. (2016), http://dx.doi.org/10.1016/j.ssnmr.2016.05.004.

[98] S. Prasad, P. Zhao, J. Huang, J.J. Fitzgerald, J.S. Shore, Niobium-93 MQMAS NMR spectroscopic study of alkali and lead niobates, Solid State Nucl. Magn. Reson. 19 (2001) 45–62, http://dx.doi.org/10.1006/snmr.2000.0022.

[99] T.F.G. Green, J.R. Yates, Relativistic nuclear magnetic resonance J-coupling with ultrasoft pseudopotentials and the zeroth-order regular approximation, J. Chem. Phys. 140 (2014) 234106, http://dx.doi.org/10.1063/1.4882678.

[100] M. Murakami, H. Yamashige, H. Arai, Y. Uchimoto, Z. Ogumi, Direct evidence of LiF formation at electrode/electrolyte interface by $^7Li$ and $^{19}F$ double-resonance solid-state NMR spectroscopy, Electrochem. Solid-State Lett. 14 (2011) A134–A137, http://dx.doi.org/10.1149/1.3609260.

[101] K. Eichele, R.E. Wasylishen, $^{31}P$ NMR study of powder and single-crystal samples of ammonium dihydrogen phosphate: effect of homonuclear dipolar coupling, J. Phys. Chem. 98 (1994) 3108–3113, http://dx.doi.org/10.1021/j100063a012.

[102] A. Bielecki, D.P. Burum, Temperature dependence of $^{207}Pb$ MAS spectra of solid lead nitrate. An accurate, sensitive thermometer for variable-temperature MAS, J. Magn. Reson. Ser. A. 116 (1995) 215–220, http://dx.doi.org/10.1006/jmra.1995.0010.

[103] P.A. Beckmann, C. Dybowski, A thermometer for nonspinning solid-state NMR spectroscopy, J. Magn. Reson. 146 (2000) 379–380, http://dx.doi.org/10.1006/jmre.2000.2171.

[104] R.P. Chapman, C.M. Widdifield, D.L. Bryce, Solid-state NMR of quadrupolar halogen nuclei, Prog. Nucl. Magn. Reson. Spectrosc. 55 (2009) 215–237, http://dx.doi.org/10.1016/j.pnmrs.2009.05.001.

[105] D.S. Middlemiss, A.J. Ilott, R.J. Clément, F.C. Strobridge, C.P. Grey, Density functional theory-based bond pathway decompositions of hyperfine shifts: equipping solid-state NMR to characterize atomic environments in paramagnetic materials, Chem. Mater. 25 (2013) 1723–1734, http://dx.doi.org/10.1021/cm400201t.

[106] F.C. Strobridge, D.S. Middlemiss, A.J. Pell, M. Leskes, R.J. Clément, F. Pourpoint, Z. Lu, J.V. Hanna, G. Pintacuda, L. Emsley, A. Samoson, C.P. Grey, Characterising local environments in high energy density Li-ion battery cathodes: a combined NMR and first principles study of $LiFe_xCo_{1-x}PO_4$, J. Mater. Chem. A. 2 (2014) 11948–11957, http://dx.doi.org/10.1039/C4TA00934G.

[107] S.J. Skinner, Characterisation of $La_2NiO_{4+\delta}$ using *in-situ* high temperature neutron powder diffraction, Solid State Sci. 5 (2003) 419–426, http://dx.doi.org/10.1016/S1293-2558(03)00050-5.

[108] P. Pyykkö, Spectroscopic nuclear quadrupole moments, Mol. Phys. 99 (2001) 1617–1629, http://dx.doi.org/10.1080/00268970110069010.

[109] C.M. Widdifield, D.L. Bryce, Solid-state $^{127}I$ NMR and GIPAW DFT study of metal iodides and their hydrates: structure, symmetry, and higher-order quadrupole-induced effects, J. Phys. Chem. A. 114 (2010) 10810–10823, http://dx.doi.org/10.1021/jp108237x.

[110] F.A. Perras, C.M. Widdifield, D.L. Bryce, QUEST—QUadrupolar Exact SofTware: a fast graphical program for the exact simulation of NMR and NQR spectra for quadrupolar nuclei, Solid State Nucl. Magn. Reson. 45–46 (2012) 36–44, http://dx.doi.org/10.1016/j.ssnmr.2012.05.002.

[111] J. Lee, G. Kim, C.P. Grey, (2016) in preparation.

[112] C. Bonhomme, C. Gervais, N. Folliet, F. Pourpoint, C. Coelho Diogo, J. Lao, E. Jallot, J. Lacroix, J.-M. Nedelec, D. Iuga, J.V. Hanna, M.E. Smith, Y. Xiang, J. Du, D. Laurencin, $^{87}Sr$ solid-state NMR as a structurally sensitive tool for the investigation of materials: antiosteoporotic pharmaceuticals and bioactive glasses, J. Am. Chem. Soc. 134 (2012) 12611–12628, http://dx.doi.org/10.1021/ja303505g.

[113] M.T. Sananes, A. Tuel, G.J. Hutchings, J.C. Volta, Characterization of different precursors and activated vanadium phosphate catalysts by $^{31}P$ NMR spin echo mapping, J. Catal. 148 (1994) 395–398, http://dx.doi.org/10.1006/jcat.1994.1221.

[114] M.T. Sananes, A. Tuel, Magnetic properties of vanadium phosphorus oxide catalysts studied by Spin Echo Mapping $^{31}P$ NMR, J. Chem. Soc., Chem. Commun. (1995) 1323–1324, http://dx.doi.org/10.1039/C39950001323.

[115] L. Canesson, A. Tuel, The first observation of "NMR-invisible phosphorus" in cobalt-substituted aluminophosphate molecular sieves, Chem. Commun. (1997) 241–242, http://dx.doi.org/10.1039/A607603C.

[116] G. Mali, A. Ristić, V. Kaučič, $^{31}P$ NMR as a tool for studying incorporation of Ni Co, Fe, and Mn into aluminophosphate zeotypes, J. Phys. Chem. B. 109 (2005) 10711–10716, http://dx.doi.org/10.1021/jp050358n.

[117] A.D. Bain, Quadrupole interactions: NMR, NQR, and in between from a single viewpoint, Magn. Reson. Chem. (2016), http://dx.doi.org/10.1002/mrc.4418.

[118] L. Zhou, M. Leskes, A.J. Ilott, N.M. Trease, C.P. Grey, Paramagnetic electrodes and bulk magnetic susceptibility effects in the *in situ* NMR studies of batteries: application to $Li_{1.08}Mn_{1.92}O_4$ spinels, J. Magn. Reson. 234 (2013) 44–57, http://dx.doi.org/10.1016/j.jmr.2013.05.011.

[119] O. Pecher, J. Carretero-Gonzalez, K.J. Griffith, C.P. Grey, Materials' methods: NMR in battery research, Chem. Mater. (2016), http://dx.doi.org/10.1021/acs.chemmater.6b03183.